Mapping light distribution in tissue by using MRI-detectable photosensitive liposomes

Citation: Simon, J., Schwalm, M., Morstein, J. et al. Mapping light distribution in tissue by using MRI-detectable photosensitive liposomes. Nat. Biomed. Eng 7, 313–322 (2023).

As Published: 10.1038/s41551-022-00982-3

Publisher: Springer Science and Business Media LLC

Persistent URL: https://hdl.handle.net/1721.1/153502

Version: Author's final manuscript: final author's manuscript post peer review, without publisher's formatting or copy editing

Mapping light distribution in tissue by using MRI-detectable photosensitive liposomes

Jacob Simon[1,&], Miriam Schwalm[1,&], Johannes Morstein[2], Dirk Trauner[2] and Alan Jasanoff[1,3,4*]

[1]Department of Biological Engineering, Massachusetts Institute of Technology, 77 Massachusetts Ave., Cambridge, MA 02139
[2]Department of Chemistry, New York University, 100 Washington Square East, New York, NY 10003
[3]Department of Brain & Cognitive Sciences, Massachusetts Institute of Technology, 77 Massachusetts Ave., Cambridge, MA 02139
[4]Department of Nuclear Science & Engineering, Massachusetts Institute of Technology, 77 Massachusetts Ave., Cambridge, MA 02139

[&]These authors contributed equally
*Corresponding author, jasanoff@mit.edu

Characterizing sources and targets of illumination in living tissue is challenging. Here we show that spatial distributions of light in tissue can be mapped by using magnetic resonance imaging (MRI) in the presence of photosensitive nanoparticle probes. Each probe consists of a reservoir of paramagnetic molecules enclosed by a liposomal membrane incorporating photosensitive lipids. Incident light causes the photoisomerization of the lipids and alters hydrodynamic exchange across the membrane, thereby affecting longitudinal relaxation-weighted contrast in MRI. We injected the nanoparticles into the brains of live rats and used MRI to map responses to illumination profiles characteristic of widely used applications of photostimulation, photometry and phototherapy. The responses deviated from simple photon propagation models and revealed signatures of light scattering and nonlinear responsiveness. Paramagnetic liposomal nanoparticles may enable MRI to map a broad range of optical phenomena in deep tissue and other opaque environments.

MRI is an attractive methodology for molecular imaging because of its almost unlimited depth penetration and relatively high spatiotemporal resolution. Molecular MRI probes have been developed for targets including small molecules, ions, enzymes, and light.[1-3] but many of these agents exhibit comparatively poor sensitivity.[4] This is particularly true of paramagnetic contrast agents visualized via their effects on longitudinal relaxation time (T_1) in the context of T_1-weighted (T_1w) MRI scans. T_1 agents induce favorable signal-brightening effects and are by far the most commonly used in the clinic, but they must usually be present at concentrations well into the micromolar range in order to produce substantial changes in image contrast.[5] This poses a particular problem in sensing applications, including photodetection, where the amount of analyte is itself often limiting.

Most previous MRI sensors have been based on T_1 contrast mechanisms in which interaction of an analyte with a single sensing or binding moiety modulates inner-sphere magnetic interactions of a single paramagnetic ion with surrounding water molecules.[6] This one-to-one actuation alters the strength of the agent's contrast effect, quantified by its longitudinal relaxivity (r_1), defined as the slope of relaxation rate ($R_1 = 1/T_1$) versus contrast agent concentration.[7, 8] Light-sensitive T_1 agents have followed this principle, wherein photoisomerization[9-11] or photocleavage[12, 13] of a single chemical group alters the relaxation dynamics arising from an individual paramagnetic center. Such agents provide limited sensitivity to light and have not been demonstrated to enable photodetection in biological tissue.

To escape the limitations of responsive MRI probes that employ one-to-one actuation, we sought a mechanism in which a unitary analyte-sensing mechanism could regulate an abundance of paramagnetic centers simultaneously, resulting in one-to-many actuation. Liposomes provide a potential basis for realizing this scenario. Encapsulation of paramagnetic MRI contrast agents such as gadoteridol in liposomes (**Fig. 1a**) is known to decrease their effective r_1, due to reduced hydrodynamic exchange between the paramagnetic metal centers and the surrounding bulk solvent.[14] Liposomes with lower solvent permeability experience reduced water exchange and lower effective r_1 per metal ion (r_{1eff}), and produce lower T_1w MRI signal than liposomes with higher permeability (**Fig. 1b**). Modulation of membrane permeability over a physically plausible range from 0 to 0.01 cm/s is expected to yield r_{1eff} values from 0 to nearly 3.8 $mM^{-1}s^{-1}$, the r_1 of unencapsulated gadoteridol at 7 T and room temperature (**Fig. 1c**).

Liposomal membranes that consist of closely packed, saturated lipids tend to block water exchange and reduce relaxivity, whereas unsaturated, fluidizing lipids facilitate water exchange and higher T_1 relaxation effects (**Fig. 1d**).[15] Dramatic differences in MRI contrast thus arise from 100 nm-diameter liposomes

formulated with varying mixes of the fluidizing lipid 1-palmitoyl-2-oleoyl-*sn*-glycero-3-phosphocholine (POPC) and the non-fluidizing 1,2-dipalmitoyl-*sn*-glycero-3-phosphocholine (DPPC) and containing 220 mM gadoteridol (**Fig. 1e**). Such liposomes enclose tens of thousands of contrast agent molecules, so we hypothesized that a concerted mechanism for reversibly regulating their permeability could provide a means for amplified analyte sensing in molecular MRI. We refer to responsive probes based on this concept as *li*po*s*omal *n*anoparticle *r*eporters (LisNRs). In this article, we describe the synthesis, characterization, and *in vivo* application of photosensitive LisNR probes, including their application for quantitative light mapping experiments in the mammalian brain.

Results

Construction of photoresponsive liposomal MRI probes. To produce light-responsive liposomal nanosensors (Light-LisNRs), we utilized 1-stearoyl-2-(4-(*n*-butyl)phenylazo-4'-phenylbutyroyl)phosphocholine (AzoPC),[16, 17] a synthetic phosphatidylcholine variant that contains the well-characterized photoisomerizable moiety azobenzene in one of its fatty acyl chains.[18] Absorption of blue light (λ_{max} = 460 nm) by AzoPC favors an extended *trans* conformation that emulates that of naturally occurring saturated lipids, whereas absorption of ultraviolet light (UV, λ_{max} = 370 nm) switches AzoPC into a kinked *cis* conformation that disrupts monolayer structure, promoting transmembrane exchange (**Fig. 2a**). We formulated liposomes using 25% AzoPC, 70% of the saturated lipid 1,2-dipalmitoyl-*sn*-glycero-3-phosphocholine (DPPC), and 5% 1,2-distearoyl-*sn*-glycero-3-phosphoethanolamine modified with polyethylene glycol (DSPE-PEG), which promotes liposome stability in suspension. These components were resuspended into a 220 mM solution of the neutral gadolinium-containing contrast agent gadoteridol, extruded through a 100 nm-mesh filter, and desalted to remove unencapsulated agent.

Photosensitivity of initial Light-LisNRs was investigated by measuring their responses to blue and UV illumination using MRI at 7 T and room temperature in microtiter plates. Relaxation rates were recorded between serially alternating one or three minute epochs of 460 nm and 370 nm irradiation delivered with approximate intensities of 0.25 and 0.1 mW/mm^2, respectively. **Fig. 2b** shows that ~30 nM probes, corresponding to 2.2 mM Gd^{3+}, undergo clear light-dependent switching. Each UV epoch produces an increase in R_1, corresponding to T_1w MRI signal brightening, and each blue illumination epoch results in decreases in R_1 and MRI signal, consistent with the higher liposome permeability expected in the presence of the UV-favored *cis*-AzoPC conformation. Over multiple cycles, however, a trend toward higher relaxation rates is evident. Gel filtration and elemental analysis revealed that multiple switching cycles results in leakage of gadoteridol from the liposomes, explaining the instability in MRI results (**Supplementary Fig. 1**). More consistent light-dependent behavior could be produced by substantially reducing the AzoPC content of the LisNR membranes (**Supplementary Fig. 2**).

To combine stability with higher relaxivity changes, we screened a set of liposome compositions for relaxation enhancement and stability to heating (**Fig. 2c**). In addition to varying concentrations of AzoPC and DPPC, we explored incorporation of longer-chain DPPC homolog 1,2-distearoyl-sn-glycero-3-phosphocholine (DSPC); 1,2-dipalmitoyl-*sn*-glycero-3-phosphoglycerol (DPPG), a charged alternative to DSPE-PEG; and cholesterol, which promotes integrity of curved bilayers. Of the conditions surveyed, we found that liposomes containing 20% AzoPC, 30% DSPC, 10% DPPG, and 40% cholesterol displayed an optimal combination of low blue-state relaxivity and stability. Liposomal probes formulated with this mixture using extrusion meshes of 100 nm and 50 nm (**Fig. 2d** and **Supplementary Fig. 3**) both displayed robust light switching behavior, but the larger probes display greater encapsulation efficiency during synthesis and were used for all subsequent studies.

Characterization of optimized Light-LisNRs. The optimized Light-LisNRs displayed markedly enhanced light switching behavior with respect to results of **Fig. 2b**. Alternating blocks of blue and UV light produce consistent R_1 values of 1.52 ± 0.04 s^{-1} and 4.52 ± 0.10 s^{-1}, respectively. This corresponds to relaxivity values of 0.69 ± 0.02 mM^{-1}s^{-1} and 2.06 ± 0.04 mM^{-1}s^{-1} following blue and UV illumination, respectively, with respect to gadolinium concentration at room-temperature and 7 T (**Fig. 2e**). The consequent light-dependent relaxivity difference of 1.37 ± 0.06 mM^{-1}s^{-1} represents a roughly five-fold improvement in dynamic range over the initial unstable Light-LisNR design of **Fig. 2b (Fig. 2e)**. Light-dependent switching also results in modest but stable changes in transverse relaxation rates (R_2) (**Supplementary Fig. 4**). The ratio of R_2 changes to R_1 changes is roughly 1:1, however, consistent with the molecular mechanism of Figure 1b and indicating that LisNRs are best visualized by T_1w MRI. Structural characterization of the optimized Light-LisNRs by dynamic light scattering (**Fig. 2f**) and transmission electron microscopy (**Fig. 2g** and **Supplementary Fig. 5**) confirms their predominantly unilamellar structure, with a mean hydrodynamic diameter of 103 ± 3 nm. This size

remains stable over a 24 hour period of incubation at 38 °C, during which no discernable R_1 changes or contrast agent leakage from the liposomes are observed (**Supplementary Fig. 6**).

The Δr_{1eff} per Gd^{3+} ion of optimized Light-LisNRs compares favorably to relaxivity changes reported previously for reversible light-responsive contrast agents.[11, 19-21] This response is moreover achieved with a ratio of about 4.3 gadoteridol molecules per photoisomerizable AzoPC molecule in each liposome, corresponding to a Δr_{1eff} value of 5.9 $mM^{-1}s^{-1}$ per photon absorbed. As a percentage of the blue light-activated r_{1eff} value the LisNR relaxivity change of more than 300% is also notable. MRI measurements performed as a function of calibrated light doses delivered to a 60 μL volume containing Light-LisNRs formulated with 2.2 mM Gd (**Fig. 2h**) show that the midpoint for both blue and UV-illuminated transitions occurs at about 2 x 10^{18} photons/mL in each case. For 370-460 nm photons used in these experiments, and assuming directional illumination of a cubic volume, this corresponds to one second of illumination at 2.8-3.5 mW/mm^2. Although the Light-LisNR probes here incorporate azobenzene chromophores that respond optimally to blue and UV light, substantial responses can also be observed using longer wavelength illumination, up to tested values of ~550 nm (**Supplementary Fig. 7**). This sensitivity reflects the broad action spectrum of the AzoPC photoswitch, and could be further modified by formulating LisNRs using alternative photoswitches tuned explicitly to longer wavelengths.[22, 23]

Assessment of Light-LisNR performance *in vivo*. Our *in vitro* results indicate the possibility that Light-LisNRs could be used for mapping experimentally relevant light distributions in live animals, a biologically important capability that has not been demonstrated using previous photosensitive MRI probes. To accomplish this, we injected the probe at a Gd^{3+} concentration of 4.4 mM over a 125 min period at 0.12 μL/min into live rat brain, targeting striatal tissue in the neighborhood of an implanted 200 μm-diameter optical fiber similar to devices used widely in optogenetics, photometry, and phototherapy procedures (**Fig. 3a**). Using T_1w gradient echo MRI at 9.4 T, we observed that LisNR injection results in effective spreading, indicated by signal increases with a full width at half maximum (FWHM) of 2.1 ± 0.5 mm (**Fig. 3b**). Interestingly, contrast distributions with similar FWHM were observed following injections of the smaller LisNR analog, suggesting that convection, rather than diffusion, is the main driver of contrast agent spreading in these experiments (**Supplementary Fig. 8**). Consistent with this explanation, probe contrast distributions were also relatively stable over time following delivery, likely reflecting extremely low expected diffusion constants on the order of 10^{-9} cm^2/s for 100 nm-diameter species.[24]

Functionality of Light-LisNRs in tissue was demonstrated by illuminating injected brain regions with blue or UV light delivered through the implanted fibers during acquisition of serial spin echo MRI scans with a frame time of 14.4 s/image. Delivery of ten minute blocks of blue light (36 ± 3 mW/mm^2 at the fiber tip) at first produced no appreciable effects, indicating that the infused LisNRs were indeed in their low relaxivity state with AzoPC molecules in the *trans* conformation (**Supplementary Fig. 9**). Application of an equivalent intensity of UV light, however, produced clear MRI signal increases in the LisNR-injected regions of three animals, which could then be reversed by subsequent application of blue light (**Fig. 3c,d**). The time courses of responses averaged over 1.6 x 1.6 mm regions around the optical fiber tips indicate that both UV and blue illumination produce signal changes that reach asymptotes within the ten-minute irradiation periods (**Fig. 3e,f**). Corresponding experiments performed with light-insensitive LisNR analogs or without illumination produced no discernable signal changes.

Quantification of these results indicates that Light-LisNRs yield mean MRI signal differences of 23 ± 3% and 21 ± 4% (mean ± SEM, $n = 3$) in response to UV and blue light, respectively, both with respect to the initial baseline (**Fig. 3g**). These changes are statistically significant (two-sided single sample *t*-test $p \leq 0.04$) and indistinguishable (paired *t*-test $p = 0.08$), indicating virtually complete reversibility. Meanwhile, control liposomal agents produce negligible changes of –1.0 ± 0.1 and 0.9 ± 0.5 to UV and blue light. MRI signal changes elicited by shorter blocks of stimulation closely track time courses observed during longer illumination periods, indicating that temporal characteristics of Light-LisNR responses *in vivo* are limited by photon delivery rates, as opposed to hysteretic behavior of the probes themselves (**Extended Data Fig. 1**). Forward and reverse contrast changes could be produced repeatedly using alternating blocks of UV and blue light, indicating stable performance similar to *in vitro* results (**Fig. 3h**). Comparison of voxel-level signal changes in two animals indicates that LisNR responses to temporally separated blocks of blue *vs.* blue or blue *vs.* UV illumination correspond closely (**Fig. 3i**), with correlation coefficients of 0.89-0.90 that are highly significant ($p < 0.0001$, $n = 338$ voxels). These results indicate the reproducibility of signal difference maps obtained using Light-LisNRs.

LisNR-based quantitative light mapping approach. The stable performance of Light-LisNRs in rat brain indicates their suitability for quantitative measurements of light intensity distribution in tissue—a capability that could critically inform optical procedures in basic science and medicine. To form light maps, we made the simplifying assumption that the rate of LisNR-mediated MRI signal changes is proportional to the rate of photon absorption; this is consistent with the approximately exponential form of the observed light response time courses and with the evidence from **Extended Data Fig. 1** that light doses largely determine the response kinetics. To test our approach, we began by examining the spatial distribution of light response rates elicited by fiber optic stimulation in a phantom containing Light-LisNRs at 2.2 mM Gd^{3+} concentration in 1% agarose gel (**Fig. 4a**). Individual voxels display light-dependent time courses that vary depending on distance from the fiber tip, and could each be fit to an equation of the form $\Delta I/\Delta I_{max} = (1 - \exp\{-kt\})$, where $\Delta I/\Delta I_{max}$ is the MRI signal change at time t, ΔI, normalized by the maximum signal change ΔI_{max}, and k is the effective rate constant for observed signal changes.

We fit the resulting maps of rate constants to a beam spreading model previously used to describe light propagation from fiber sources in brain tissue.[25] Under low-scattering and non-absorptive conditions comparable to our gel phantom, the model yields characteristic conical profiles (**Fig. 4b**). We surveyed a regular grid of possible scattering and anisotropy coefficients, μ_s = 10-150 cm^{-1} and g = 0.95-0.99, respectively, while setting the attenuation coefficient to zero and integrating over a volume corresponding to the imaging data in each case. Notably, in order to achieve good correspondence between data and models, it is necessary also to impose a maximum value on the beam spreading intensities prior to integrating them over the imaging region. Such a nonlinearity could arise if Light-LisNRs in areas of high photon flux exhibit saturating response rates at sub-voxel resolution.

Fig. 4c shows that experimental rate constant maps and corresponding optimized models share qualitative features with one another. In particular, both data and models display elongated regions of peak k values somewhat below the fiber tip, and both blue response maps extend further than the UV profiles, with a more conical shape than the UV maps. These results are reproducible and are presented for a second phantom in **Supplementary Fig. 10**. Mean correlation coefficients between data and models are 0.90 ± 0.00 and 0.91 ± 0.02 for UV and blue illumination, respectively. Mean optimized values of μ_s = 130 ± 20 cm^{-1} and g = 0.98 ± 0.00 for UV and μ_s = 60 ± 10 cm^{-1} and g = 0.99 ± 0.00 for blue were obtained. These results are consistent with the higher degree of scattering expected for UV versus blue light and validate our strategy of volumetric light mapping using Light-LisNRs in MRI.

Spatially resolved light mapping in brain tissue. We next used the rat brain MRI data of **Fig. 3** to compute maps of responses to UV and blue illumination in brain tissue, where biomedical applications of fiber-based light delivery are particularly important. Light response time courses were obtained from individual voxels for which signal change amplitudes of 10% or more were observed. Although these time courses are noisier than the analogous data from phantoms, spatial dependence of light response characteristics can be observed (**Fig. 4d**). Response rate values are not correlated (R = –0.013, p = 0.66) with response amplitudes, reflective of probe concentrations, and light response rates vary differently from response amplitudes as a function of distance from the fiber tip (**Extended Data Fig. 2a,b**). This indicates that variability in light response rates is not strongly affected by heterogeneity of probe distributions in the brain. Distributions of light response rates are also consistent over repeated illumination cycles, indicating that fitted values are stable over time (**Extended Data Fig. 2c,d**). Response rate maps computed from the data do reveal variation across animals (**Fig. 4e**), however, as reflected by mean k values that range from 0.013 s^{-1} to 0.027 s^{-1} in regions surrounding optical fiber tips (**Fig. 4f**). This variability likely arises in part from differences in fiber placement with respect to the image slice and LisNR distribution, as well as differences in the propagation of light through tissue for each animal. A notable point of commonality among the profiles shown is the presence of nonzero k values above the fiber tip positions. This indicates that fiber-based illumination spreads broadly in tissue and suggests a greater role for photon diffusion than assumed by some light propagation models.[25-27]

UV and blue light response rates from six animals were combined into maps of average k values for every voxel where measurements from two or more animals were obtained. These data were fit to a hybrid model consisting of a beam spreading function in linear combination with a homogeneous photon diffusion term (**Fig. 4g**).[28] A grid search was performed over μ_s values from 100-300 cm^{-1} and g values from 0.7 to 0.95 to determine which combinations best fit the mean light response maps. As with the phantom calculations, a nonlinearity was applied prior to integration over the imaging volume, and the relative amplitudes of diffusive and beam spreading components were also optimized in each case.

A comparison of the mean experimental maps and corresponding optimal models is shown in **Fig. 4h**. Qualitative features common to both data and models include (1) the more symmetric, diffuse appearance of the UV data compared with the blue, consistent with reduced propagation of UV light expected in tissue; (2) ellipsoids of peak *k* values extending several hundred microns below the fiber tips, again reflecting saturation of light responses at areas closest to the fiber tip; and (3) nonzero *k* values above the fiber tips, paralleling observations from individual animals in **Fig. 4e** and confirming that diffusive light spreading contributes to the results. A model with μ_s = 220 cm^{-1} and g = 0.8 best fit the UV data; with these parameters, correlation coefficients of 0.65 and 0.70 are calculated for beam spreading and diffusive model components separately and 0.83 for the hybrid model overall. For blue illumination, the best fit is achieved with μ_s = 240 cm^{-1} and g = 0.85; correlation coefficients of 0.78 and 0.42 are observed for beam spreading and diffusive components, respectively, and 0.83 for the complete model. Fitted values of μ_s and g are similar to previously reported quantities, but do not strongly distinguish blue and UV illumination. Instead, the greater tissue scattering associated with UV light is explained by the balance of model components. Assuming independence of fitted voxel-wise *k* values (n = 286 for UV and 299 for blue), the correlation of the data to photon diffusion contributions is significantly higher for UV illumination data than for blue (Z = 5.0, $p < 10^{-5}$), while the correlation to beam spreading contributions is lower for UV (Z = –3.2, p = 0.0013).

Discussion

This work introduces a sensor architecture for MRI and its application to mapping photon distributions relevant to important optical approaches from basic science to clinical practice. The sensors employ reversible analyte-dependent modulation of liposome membrane water permeability to regulate contrast effects arising from encapsulated contrast agent molecules. Resulting photosensitive Light-LisNR probes harness the robustness and amplification factor afforded by the LisNR contrast principle to produce quantifiable light-dependent responses *in vitro* and *in vivo*. We use Light-LisNRs to produce maps of light propagation through phantoms and complex mammalian brain tissue. The results can be analyzed using a quantitative modeling approach and reveal that photon diffusion and local saturation of chromophores both contribute to LisNR-mediated response profiles in tissue. Because of the similarity of LisNR sensors to photoresponsive actuators and the widespread application of fiber-based optical techniques in biomedicine,[29] the phenomenology we describe could be directly useful for planning procedures and interpreting experimental findings in a range of situations. No other method currently provides similar capability for minimally invasive light detection in deep tissue.

Future applications of Light-LisNRs could include MRI-assisted optical imaging in many contexts. These include mapping of light delivery by invasive or noninvasive techniques. Improved light mapping results might be obtained using higher LisNR concentrations, more homogeneous delivery,[30] and higher resolution MRI measurements, which would permit better sampling of the light response rates and more accurate determination of fiber tip locations. Further applications could also be reached by modifying the probes themselves. LisNRs could potentially be enhanced by tuning their action spectrum to different wavelengths,[22, 23] improving their absorption cross-section,[31] or boosting their relaxivity changes using alternative contrast agent encapsulation parameters. This could enable them to image a broader range of optical sources in tissue, including fluorescent or bioluminescent molecules. Formulating LisNRs with smaller size or conjugation of targeting moieties could be used to improve distribution and delivery of the probes *in vivo*, or to alter their propensity to undergo cell internalization.[32] Importantly, the LisNR mechanism can readily be adapted to incorporate alternative approaches for reversible membrane permeabilization that go beyond the AzoPC-dependent light sensing strategy applied here. Using ligand-gated pore structures, for instance, we anticipate that LisNRs could be adapted for sensing a variety of chemical analytes of interest in biomedicine.

Methods

Modeling of LisNR contrast properties. To model the relationship between r_{1eff} and bilayer water permeability for paramagnetic liposomes, we used a two compartment model.[14] This model is valid for relatively small volume fractions ($f \leq 10\%$), as it neglects the signal contribution of intraliposomal water protons. This assumption is valid for all experimental conditions used in this paper, which involved liposomes at $f \leq 1\%$. The two-compartment model also assumes that diffusion of water molecules within liposomes does not contribute to the time constant for water exchange between liposomes and bulk solvent. Under these conditions, the effective relaxivity of encapsulated contrast agents can be computed using:

$$\tau = {}^{d}/_{6P} \qquad (1)$$

$$r_{1eff} = \frac{r_1}{1+\tau \cdot c r_1} \quad (2)$$

where d is the liposome diameter in cm, P is the liposomal membrane permeability in cm/s, τ is the exchange lifetime in s, r_1 is the relaxivity of unencapsulated agent in mM/s, and c is the intraliposomal contrast agent concentration in mM. Plots of r_{1eff} *vs.* d computed over a range of P values are presented in **Fig. 1c**.

Paramagnetic liposome formulation. Lipids were purchased from Avanti Polar Lipids (Alabaster, AL), unless noted otherwise. AzoPC was synthesized as described previously.[17] Most other chemicals were purchased from MilliporeSigma (St. Louis, MO).

To form vesicles, lipid mixes (1.65 μmol total) were first co-dissolved in chloroform or 97/2/1 (v/v) chloroform/methanol/water (phosphatidyl glycerols only) and dried overnight under high vacuum. Each resulting lipid film was stored until use at –20 °C in a vial sealed with a teflon septum and parafilm, contained in a sealed secondary container loaded with calcium sulfate. Lipids were resuspended by adding 1.1 mL of a gadoteridol solution (Bracco, Milan, Italy) containing 220 mM Gd^{3+} to each film. Resulting suspensions were incubated at 58 °C in a water bath for at least two hours with brief vortexing every 10-20 minutes. Each solution was subjected to three freeze-thaw cycles using liquid nitrogen. Samples were subsequently processed using a liposome extrusion kit from Avanti Polar Lipids, which uses 1 mL syringes to force the aqueous lipid solution through polycarbonate filters of defined pore size. To form LisNRs and LisNR analogs described here, lipid solutions were forced through double-stacked 100 nm or 50 nm filters 21 times while maintaining temperatures above ~60 °C using a heating block.

Resulting liposome solutions were purified from unencapsulated gadoteridol by gravity-flow size exclusion column chromatography, using Sepharose CL-4B resin purchased from Cytiva (Marlborough, MA) with a buffer containing 10 mM 4-(2-hydroxyethyl)-1-piperazineethanesulfonic acid (HEPES), pH 7.4, plus 139 mM NaCl.

Liposome characterization. Metal concentrations in purified liposome solutions were quantified using an Agilent inductively coupled mass spectrometry (ICP-MS) instrument in the MIT Center for Environmental Health and Safety, with respect to standards containing 0-1000 ppb gadolinium and 10 ppb erbium as an internal standard. The fraction of free contrast agent remaining after purification or after heat stability tests was determined by further size exclusion chromatography and ICP-MS of liposome-associated (early) and free contrast agent (late) fractions. Liposome solutions were stored in the dark at 4 °C for up to several months.

Liposome sizes were characterized by dynamic light scattering (DLS) and transmission electron microscopy (TEM). DLS was performed using a Wyatt Technology (Goleta, CA) DynaPro DLS instrument. Samples were formulated at 50 μM Gd^{3+} and results displayed as a mass-weighted histogram of sizes computed with minimal degrees of freedom from the raw scattering data. For TEM, 3 μL of LisNR solution containing 5-6 mM Gd^{3+} was dropped on a lacey copper grid coated with a continuous carbon film and blotted to remove excess sample without damaging the carbon layer by Gatan (Pleasanton, CA) Cryo Plunge III. The grid was mounted on a Gatan 626 single tilt cryo-holder. The specimen and holder tip were then cooled down by liquid-nitrogen. Imaging was performed on a JEOL (Tokyo, Japan) 2100 FEG microscope using a minimum energy dose chosen to avoid sample damage under the electron beam. The microscope was operated at 200 kV and with magnification in the ranges from 10,000-60,000x to assessing particle size and distribution. All images were recorded on a Gatan 2kx2k UltraScan CCD camera.

Light sources. For *in vitro* experiments performed in buffer, with the exception of light titrations, light was delivered using UV (365 nm, 8 mW output) and blue (460 nm, 25 mW output) LED flashlights (Amazon standard identification numbers B00KJLRU6W and B001TIEHO2, respectively). Light intensity was determined using a digital optical power meter, UV-compatible sensor, and neutral density filters to decrease intensity, all purchased from Thorlabs (Newton, NH). Light intensities were computed by dividing the power meter readings by the total sensor area (71 mm^2).

Illumination for experiments *in vivo* and in agarose phantoms, as well as for *in vitro* light titrations, was delivered via a multimode optical fiber with a core diameter of 200 μm and a numerical aperture of 0.39, purchased from from Thorlabs (Newton, NJ). For experiments *in vivo*, the fiber delivering either ultraviolet or blue light for liposome activation/inactivation was inserted, after removing the cladding from the tip, via a craniotomy and glued to the skull with biocompatible UV glue. The amount of glue used to hold the fiber in

place was kept at a minimum, to reduce the potential for artifacts in MRI. During the MRI experiments the fiber was connected to a UV or blue light source. For UV illumination, we used a 365 nm LED from Thorlabs; for blue, we used a 470 nm LED from NPI (Tamm, Germany). These were located outside the scanner room. Fibers were connected via an SMA connector to either the blue or UV light sources. Timing of the illumination periods was controlled by manually switching on the appropriate light source. Illumination intensities at the fiber tip were calculated by measuring total power output from the fiber using an optical power meter (Thorlabs) and dividing by the fiber cross-sectional area.

MRI of formulations in buffer. Imaging was performed on a 7 T small animal scanner (Bruker Biospin, Billerica, MA) using a 70 cm inner diameter linear volume coil (Bruker). Scanner operation was controlled using the ParaVision 5.1 software (Bruker). T_1-mapping experiments were performed using a series of spin-echo scans with (TE) = 8 ms, matrix size = 256 × 256, field of view (FOV) = 50 mm × 50 mm, and slice thickness = 2 mm, with repetition times (TR) of 30, 75, 116, 186, 298, 477, 763, 1221, 1953, 3125, and 5000 ms. The number of scan averages was set such that the total scan time at each TR was at least 7 minutes. Raw k-space data were reconstructed and analyzed using a custom script in MATLAB (Mathworks, Natick, MA). R_1 values were obtained by exponential fitting to MRI data obtained as a function of TR, and r_{1eff} values were obtained by dividing R_1 values from background by metal concentrations determined by ICP-MS.

To calculate the reported value of r_{1eff} per isomerization event, we used the intramolecular concentration of 220 mM Gd^{3+} and an intralumenal volume of $4/3\pi(d/2)^3$ for d = 100 nm, leading to an estimate of about 69,000 gadolinium agents per vesicle; we also used a membrane surface area of $4\pi(d/2)^2$ for d = 100 nm and an area of 0.75 nm^2 per lipid headgroup, leading to estimates of about 80,000 lipids per vesicle and 16,000 AzoPC molecules per vesicle, or approximately 4.3 Gd^{3+} ions per AzoPC. Animal procedures. Adult male Sprague-Dawley rats (350–450 g) were purchased from Charles River Laboratories (Wilmington, MA). After arrival, animals were housed and maintained on a 12 hour light/dark cycle and permitted ad libitum access to food and water. All procedures were carried out in strict compliance with National Institutes of Health guidelines, under oversight of the Committee on Animal Care at the Massachusetts Institute of Technology.

Preparation of animals for *in vivo* MRI. Animals were anesthetized with isoflurane (3% for induction, 2% for maintenance) and placed on a water heating pad from Braintree Scientific (Braintree, MA) to maintain body temperature at 37 °C. Animals were then positioned in a stereotaxic frame and topical lidocaine was applied to the scalp before a 3 cm lateral incision extending from bregma to lambda was made, exposing the skull. Craniotomies (0.5 mm) were drilled bilaterally over the caudate-putamen (CPu), 0.5 mm anterior and 3.0 mm lateral to bregma. A 28-gauge infusion cannula was lowered to approximately 6.5 mm below the surface of the skull through each craniotomy and held in place using the stereotaxic arms.

Light-LisNRs (20% AzoPC, 30% DSPC, 40% cholesterol, 20% DPPG) or light-insensitive LisNR control analogs (20% POPC, 30% DSPC, 40% cholesterol, 20% DPPG), were infused via the cannulae over the course of 2 hours with an injection rate of 0.125 μL/min (15 μL total), at a volume fraction of 2%, equivalent to 4.4 mM Gd^{3+} or ~65 nM liposomes. Ten minutes after the injection was completed, infusion cannulae were slowly removed from the brain and the craniotomies were closed with bone wax (CP Medical, Inc. Portland, OR). The optical fiber was lowered through a third craniotomy (3.0 mm posterior and +3.00 mm lateral to bregma) in an orientation that paralleled the midline plane with a 20° angle down and toward the rostral end. Animals were then transferred into a custom rat imaging cradle, fixed in place with ear bars and a bite bar, maintained under 2% isoflurane anesthesia, and kept warm using a recirculating water heating pad for the duration of imaging.

Imaging in rats and phantoms. MRI was performed on a Bruker 9.4 T BioSpec small animal scanner equipped with a Bruker transmit-only 70 cm inner diameter linear volume coil and a Bruker receive-only three-channel array coil with openings through which the optical fibers were led. Scanner operation was controlled using the ParaVision 6.01 software from Bruker.

Multislice T_1w fast low-angle-shot (FLASH) MRI images were acquired to evaluate the spread of liposomes with TE = 4 ms, TR = 200 ms, matrix size 150 mm × 90 mm, FOV = 30 mm × 18 mm, flip angle = 70°, and four coronal slices with slice thickness = 1 mm. Sagittal T_2-weighted (T_2w) rapid aquisition with refocused echoes (RARE) scans with TE = 30 ms, TR = 1000 ms, five averages, RARE factor = 8, matrix size = 256 × 256, FOV = 25.6 mm × 25.6 mm, and slice thickness = 1 mm (4 slices) were used along with the FLASH images to evaluate the fiber positions.

A T_1w RARE pulse sequence was used for time-resolved imaging of light responses or control dynamics, using the following parameters: TE = 5 ms, TR = 300 ms, RARE factor = 4, three averages, matrix size = 128 × 64, FOV = 30 mm × 18 mm, and four coronal slices with slice thickness = 1 mm. Each scan lasted 14.4 s. Scan series of different durations and with different on and off periods of blue or UV illumination were performed, with timing as specified in the text.

Analysis of *in vivo* MRI data. Multichannel MRI data were reconstructed in ParaVision and then exported to MATLAB, where subsequent processing was performed. Time-resolved data were interpolated to an in-plane resolution of 125 μm × 125 μm. Elimination of non-brain voxels was performed using a manual segmentation routine. Centroids of contrast enhancement were manually identified from T_1w FLASH and RARE scans; these centroids were used both for quantitative estimation of contrast agent spreading and for positioning of ROIs from which stimulus-free time courses were obtained. Meanwhile, ROIs for analysis of responses to light stimulation were defined with respect to fiber tip positions determined by close examination of coronal FLASH and sagittal T_2w RARE scans.

Signal change time courses and signal difference amplitudes were computed over 1.6 × 1.6 mm ROIs. Time courses are presented as percent signal change (%SC) with respect to prestimulation baseline periods of 10 scans each (I_0), such that %SC = 100 × ($I - I_0$)/I_0, for signal intensities I. Percent signal differences (%SD) between MRI intensities pre *vs.* post illumination (I_{pre} vs. I_{post}) presented in maps and dot plots were computed from intervals of 10 scans each with respect to minimum values (I_{min}) either prior to UV illumination or after blue illumination, such that %SD = 100 × $|I_{pre} - I_{post}|/I_{min}$.

Light mapping analysis. Light response rate constants k were computed from signal change data by fitting single-voxel MRI signal time courses to the equation: $\Delta I/\Delta I_{max} = (1 - \exp\{-kt\})$, where $\Delta I = I - I_{pre}$ for signal I at time t, and $\Delta I_{max} = I_{post} - I_{pre}$. Fitting was performed using nonlinear least squares optimization in MATLAB. Fits were considered reliable for voxels with signal changes of 10% or more and where k values were determined to lie between $1/dt$ and $1/t_{max}$, where dt is the sampling interval of the MRI time courses (14.4 s) and t_{max} is the duration of the relevant illumination block (5-10 min). k maps were computed over ROIs defined around the fiber tip locations in each animal or phantom. Mean values of k were computed for voxels where two or more animals contributed, based on criteria defined above; all other voxels were excluded from analysis.

A MATLAB-based implementation of a beam spreading function,[25] generously shared by Guy Yona and Shy Shoham, was used to fit experimental light mapping data. To model data from phantoms, relative photon intensity maps $M(\mu_s, g)$ were computed using an index of refraction of 1.34, numerical aperture 0.39, fiber radius 100 μm, attenuation coefficient $\mu_a = 0$, scattering coefficients μ_s = 10 to 150 cm^{-1} in intervals of 10 cm^{-1}, and scattering anisotropies from 0.95 to 0.99 in intervals of 0.01. To model data from rat brains, relative photon intensity maps $M(\mu_s, g)$ were computed using an index of refraction of 1.36, numerical aperture 0.39, fiber radius 100 μm, attenuation coefficient $\mu_a = 0$, scattering coefficients μ_s = 100 to 300 cm^{-1} in intervals of 20 cm^{-1}, and scattering anisotropies from 0.70 to 0.95 in intervals of 0.05. For rat brain data, a photon diffusion profile P was calculated using a standard formulation[28] adapted for $\mu_a = 0$ as $\phi_D = 3\mu_s/4\pi r$, where r is the distance from a point source. P was generated by convolution of ϕ_D with the fiber geometry followed by normalization, which eliminates dependence on μ_s. All models were computed with a spatial resolution of 40 μm prior to integration over voxel volumes.

Modeled values of the light response rate constants k (denoted as k_m) were computed according to the following expression:

$$k_m(x,y) = \int_{V(x,y)} \min\left[aM(\mu_s, g) + bP, c\right] dxdy \qquad (3)$$

Here, the integral denotes integration of the light spreading models over the corresponding voxel volumes $V(x,y)$ for each voxel position (x, y) in the two-dimensional light response maps of **Fig. 4**. For each combination of μ_s and g, the constants a, b, and c in the above expression were optimized by nonlinear least squares fitting between the experimental and modeled k values; the min operation with respect to c imposes the nonlinear relationship between light intensity and LisNR response rate discussed in the text. Values of μ_s and g that gave rise to optimal fits are reported, and comparisons of experimental and modeled maps are presented.

Reporting Summary. Further information on research design is available in the Nature Research Reporting Summary linked to this article.

Data availability
Source data for graphs appearing in the main text and extended data figures are provided.

References

1. Tu, C. & Louie, A.Y. Strategies for the development of gadolinium-based 'q'-activatable MRI contrast agents. *NMR Biomed* **26**, 781-787 (2013).
2. Lux, J. & Sherry, A.D. Advances in gadolinium-based MRI contrast agent designs for monitoring biological processes in vivo. *Curr Opin Chem Biol* **45**, 121-130 (2018).
3. Wei, H., Frey, A.M. & Jasanoff, A. Molecular fMRI of neurochemical signaling. *J Neurosci Methods* **364**, 109372 (2021).
4. Angelovski, G. What We Can Really Do with Bioresponsive MRI Contrast Agents. *Angew Chem Int Ed Engl* **55**, 7038-7046 (2016).
5. Boros, E., Gale, E.M. & Caravan, P. MR imaging probes: design and applications. *Dalton Trans* **44**, 4804-4818 (2015).
6. Li, H. & Meade, T.J. Molecular Magnetic Resonance Imaging with Gd(III)-Based Contrast Agents: Challenges and Key Advances. *J Am Chem Soc* **141**, 17025-17041 (2019).
7. Lauffer, R.B. Paramagnetic metal complexes as water proton relaxation agents for NMR imaging: Theory and design. *Chem Rev* **87**, 901-927 (1987).
8. Wahsner, J., Gale, E.M., Rodriguez-Rodriguez, A. & Caravan, P. Chemistry of MRI Contrast Agents: Current Challenges and New Frontiers. *Chem Rev* **119**, 957-1057 (2019).
9. Venkataramani, S. et al. Magnetic bistability of molecules in homogeneous solution at room temperature. *Science* **331**, 445-448 (2011).
10. Tu, C. & Louie, A.Y. Photochromically-controlled, reversibly-activated MRI and optical contrast agent. *Chem Commun (Camb)*, 1331-1333 (2007).
11. Gao, M. et al. Synthesis and Comparative Evaluation of Photoswitchable Magnetic Resonance Imaging Contrast Agents. *ACS Omega* **5**, 14759-14766 (2020).
12. Reessing, F. et al. A light-responsive liposomal agent for MRI contrast enhancement and monitoring of cargo delivery. *Chem Commun (Camb)* **55**, 10784-10787 (2019).
13. Reessing, F. et al. A Photocleavable Contrast Agent for Light-Responsive MRI. *Pharmaceuticals (Basel)* **13** (2020).
14. Koenig, S.H. et al. Permeability of liposomal membranes to water: results from the magnetic field dependence of T1 of solvent protons in suspensions of vesicles with entrapped paramagnetic ions. *Magn Reson Med* **23**, 275-286 (1992).
15. Terreno, E. et al. Determination of water permeability of paramagnetic liposomes of interest in MRI field. *J Inorg Biochem* **102**, 1112-1119 (2008).
16. Morgan, C.G., Sandhu, S.S., Yianni, Y.P. & Dodd, N.J. The phase behaviour of dispersions of Bis-Azo PC: photoregulation of bilayer dynamics via lipid photochromism. *Biochim Biophys Acta* **903**, 495-503 (1987).
17. Pernpeintner, C. et al. Light-Controlled Membrane Mechanics and Shape Transitions of Photoswitchable Lipid Vesicles. *Langmuir* **33**, 4083-4089 (2017).
18. Morstein, J., Impastato, A.C. & Trauner, D. Photoswitchable Lipids. *Chembiochem* **22**, 73-83 (2021).
19. Osborne, E.A., Jarrett, B.R., Tu, C. & Louie, A.Y. Modulation of T2 relaxation time by light-induced, reversible aggregation of magnetic nanoparticles. *J Am Chem Soc* **132**, 5934-5935 (2010).
20. Kruttwig, K. et al. Reversible low-light induced photoswitching of crowned spiropyran-DO3A complexed with gadolinium(III) ions. *Molecules* **17**, 6605-6624 (2012).
21. Dommaschk, M. et al. Photoswitchable Magnetic Resonance Imaging Contrast by Improved Light-Driven Coordination-Induced Spin State Switch. *J Am Chem Soc* **137**, 7552-7555 (2015).
22. Dong, M., Babalhavaeji, A., Samanta, S., Beharry, A.A. & Woolley, G.A. Red-Shifting Azobenzene Photoswitches for in Vivo Use. *Acc Chem Res* **48**, 2662-2670 (2015).
23. Chander, N. et al. Optimized Photoactivatable Lipid Nanoparticles Enable Red Light Triggered Drug Release. *Small* **17**, e2008198 (2021).
24. Thorne, R.G. & Nicholson, C. In vivo diffusion analysis with quantum dots and dextrans predicts the width of brain extracellular space. *Proc Natl Acad Sci U S A* **103**, 5567-5572 (2006).
25. Yona, G., Meitav, N., Kahn, I. & Shoham, S. Realistic Numerical and Analytical Modeling of Light Scattering in Brain Tissue for Optogenetic Applications(1,2,3). *eNeuro* **3** (2016).
26. Aravanis, A.M. et al. An optical neural interface: in vivo control of rodent motor cortex with integrated fiberoptic and optogenetic technology. *J Neural Eng* **4**, S143-156 (2007).
27. Acker, L., Pino, E.N., Boyden, E.S. & Desimone, R. FEF inactivation with improved optogenetic methods. *Proc Natl Acad Sci U S A* **113**, E7297-E7306 (2016).

28. Wang, L.V. & Wu, H.-I. Biomedical Optics: Principles and Imaging. (Wiley-Interscience, Hoboken, NJ; 2007).
29. Canales, A., Park, S., Kilias, A. & Anikeeva, P. Multifunctional Fibers as Tools for Neuroscience and Neuroengineering. *Acc Chem Res* **51**, 829-838 (2018).
30. Ghosh, S., Harvey, P., Simon, J.C. & Jasanoff, A. Probing the brain with molecular fMRI. *Curr Opin Neurobiol* **50**, 201-210 (2018).
31. Cabre, G. et al. Rationally designed azobenzene photoswitches for efficient two-photon neuronal excitation. *Nat Commun* **10**, 907 (2019).
32. Hai, A., Cai, L.X., Lee, T., Lelyveld, V.S. & Jasanoff, A. Molecular fMRI of Serotonin Transport. *Neuron* **92**, 754-765 (2016).

Acknowledgements
This research was funded by NIH grants R21 DA044748 and R01 NS120592, and a grant from the G. Harold and Leyla Y. Mathers Foundation to AJ. JS was supported by a Friends of the McGovern Fellowship from the McGovern Institute for Brain Research and by the MIT Neurobiological Engineering Training Program (NIH T32 EB019940). MS was the recipient of a Marie Curie Individual Fellowship from the European Commission. The authors are grateful to Guy Yona and Shy Shoham for advice about light modeling and for sharing code for computing beam spreading profiles.

Author contributions
JS and AJ developed the LisNR concept. JS, MS, and AJ designed the research. JS performed and analyzed the *in vitro* experiments. MS performed the *in vivo* experiments. MS and AJ analyzed the *in vivo* data. JM and DT synthesized and characterized AzoPC and advised on *in vitro* light response experiments. JS, MS, and AJ wrote the paper.

Competing interests
The authors declare no competing interests.

Additional information [please do not modify this block of text]
Extended data is available for this paper at https://doi.org/10.1038/s41551-02X-XXXX-X.
Supplementary information The online version contains supplementary material available at https://doi.org/10.1038/s41551-02X-XXXX-X.
Correspondence and requests for materials should be addressed to
Peer review information *Nature Biomedical Engineering* thanks Reviewer and the other, anonymous, reviewer(s) for their contribution to the peer review of this work. Peer reviewer reports are available.
Reprints and permissions information is available at www.nature.com/reprints.

Figure captions

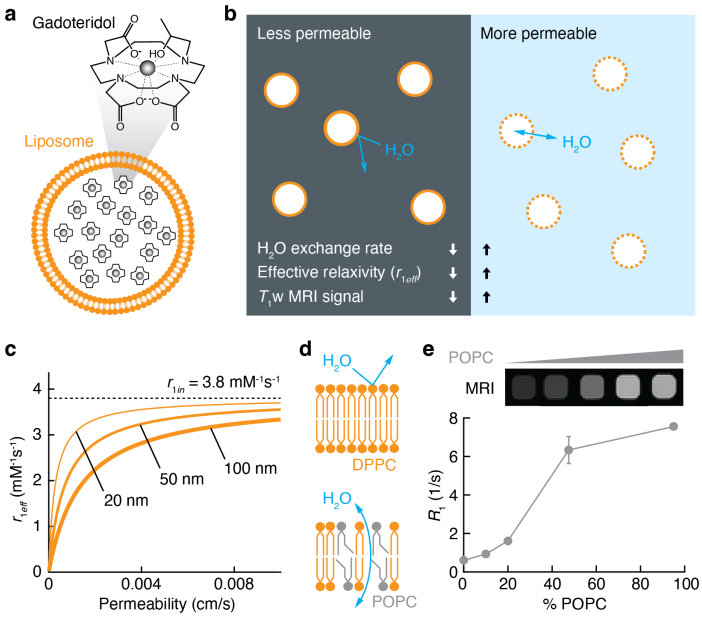

Fig. 1 | Principle of liposomal nanoparticle reporters. a, LisNRs are formulated by enclosing a high concentration of MRI contrast agents such as gadoteridol (shown) in a liposomal membrane with regulable water permeability (orange). **b,** In their more permeable form, LisNRs support greater water exchange, leading to a higher effective relaxivity (r_{1eff}) and greater T_1-weighted (T_1w) MRI signal. **c,** Two compartment modeling enables estimation of r1eff as a function of permeability and liposomal diameter. All r_{1eff} curves range from zero at low permeability to the r_1 value of unencapsulated gadoteridol at high permeability (dashed line). **d,** Liposomal membranes including unsaturated lipids such as POPC (bottom) display higher water permeability than membranes composed of fully saturated lipids such as DPPC (top). **e,** Experiments indicate the dynamic range of MRI signal differences for LisNR analogs formulated at 2.2 mM $Gd^{3+}$with increasing POPC concentrations (top), with corresponding underlying T_1 relaxation rates (R_1) graphed at bottom. All lipid compositions also contain 5% DSPE-PEG. Error bars denote SD of 4 technical replicates.

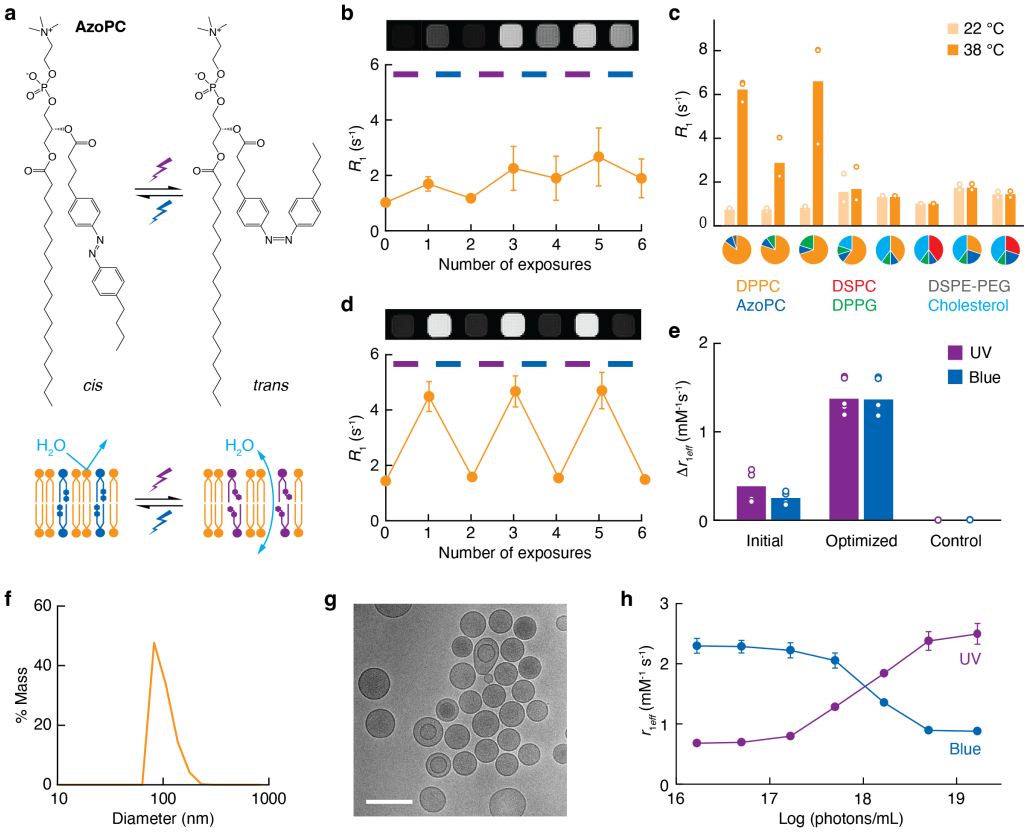

Fig. 2 | Formation and *in vitro* characterization of Light-LisNRs. a, Light-LisNRs incorporate AzoPC, a modified lipid molecule that undergoes photoconversion between a blue light-favored *cis* state (right) and a UV light-favored *trans* state (left). The *cis* state emulates unsaturated lipids and promotes water permeability (bottom right), whereas the *trans* state emulates saturated lipids and opposes water permeability (bottom left). **b,** Initial Light-LisNRs formulated with 25% AzoPC and 2.2 mM Gd^{3+} undergo clear light-dependent switching with R_1 values following repeated epochs of UV and blue illumination (colored bars) graphed at bottom and corresponding T_1w MRI images at top. The trend toward higher R_1 after repeated switching arises from gadoteridol leakage (see text). **c,** Lipid compositions were screened for stability by examining R_1 values for LisNR analogs at two temperatures. Differences between the conditions suggest leakage. **d,** Performance of optimized LisNRs under repeated cycles of UV and blue illumination, showing T_1w MRI signal (top) and corresponding R_1 values (bottom). **e,** Comparison of relaxivity changes displayed by initial and optimized LisNRs, showing improved characteristics; control liposomes formulated without AzoPC show no appreciable light responses. **f,** Mass-weighted histogram showing size distribution of LisNRs measured by dynamic light scattering. **g,** Electron micrograph of LisNRs showing predominantly unilamellar structure. Scale bar = 200 nm. **h,** Effective relaxivity as a function of UV or blue photon dose per volume for LisNRs formulated at 2.2 mM Gd^{3+}, following blue or UV saturation, respectively. All error bars denote SD of at least $n = 3$ technical replicates.

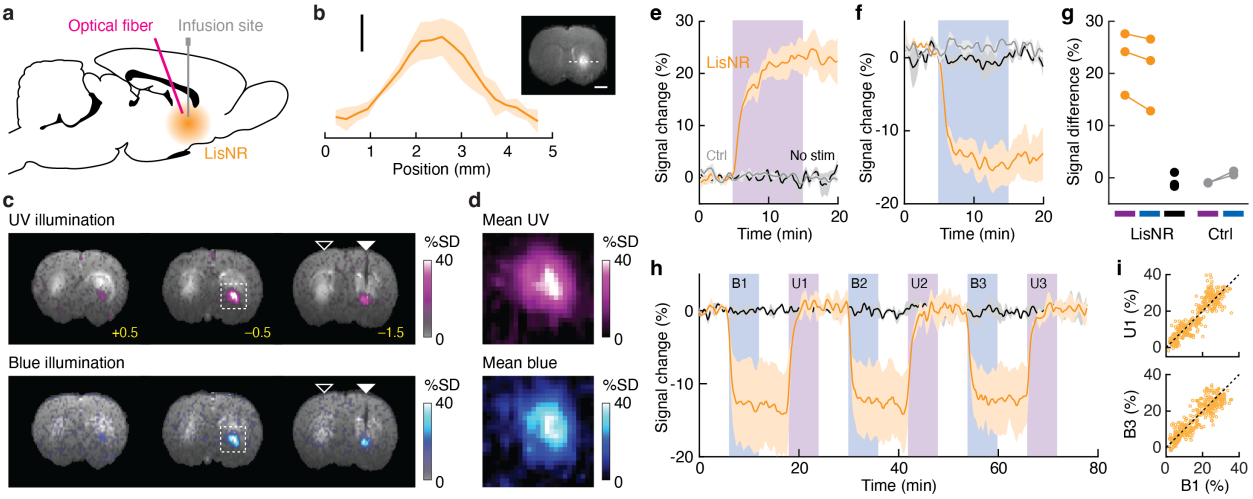

Fig. 3 | Assessment of Light-LisNR performance *in vivo*. a, Geometry of injection and fiber based optical stimulation used for evaluation of Light-LisNRs *in vivo*. **b,** Contrast enhancement by injected LisNRs as a function of lateral position, along dashed lines from individual images as shown for a representative animal in the inset (scale bar = 2 mm). Shading = SD for $n = 6$ biological replicates, vertical bar = 50% signal. **c,** Coronal MRI scans from a representative animal showing contrast enhancement from Light-LisNR infusion, with colored overlays denoting signal differences observed following UV illumination (top) or blue illumination (bottom). Positions of the optical fiber used for stimulation and contralateral unstimulated area are denoted by closed and open arrowheads, respectively. Bregma coordinates labeled in yellow. **d,** Closeups of injected regions (dashed boxes in **c**), with signal differences averaged over three animals, showing equivalent differences observed following UV (top) and blue (bottom) illumination. **e,** Signal change *vs.* time before, during, and after UV irradiation (purple shading) of injected Light-LisNRs (orange) or control liposomes (gray), with time course of unstimulated LisNRs shown in black. Shaded margins denote SEM of $n = 3$ (LisNRs) or $n = 2$ (control liposomes) biological replicates. **f,** Equivalent data for blue light illumination (blue shading). **g,** Mean signal differences produced by UV (purple), blue, or null (black) illumination observed in LisNR-injected or control liposome-injected (Ctrl) brain regions. **h,** Data from two animals showing mean responses to alternating epochs of blue and UV illumination (orange), along with corresponding unstimulated control time course (black). Shading denotes SEM of $n = 2$ biological replicates. **i,** Scatter plots derived from labeled illumination periods in **h**, showing correlation of voxel-level responses (one dot per voxel per animal) between first blue and first UV stimulation periods (top) and between first and last blue illumination periods (bottom).

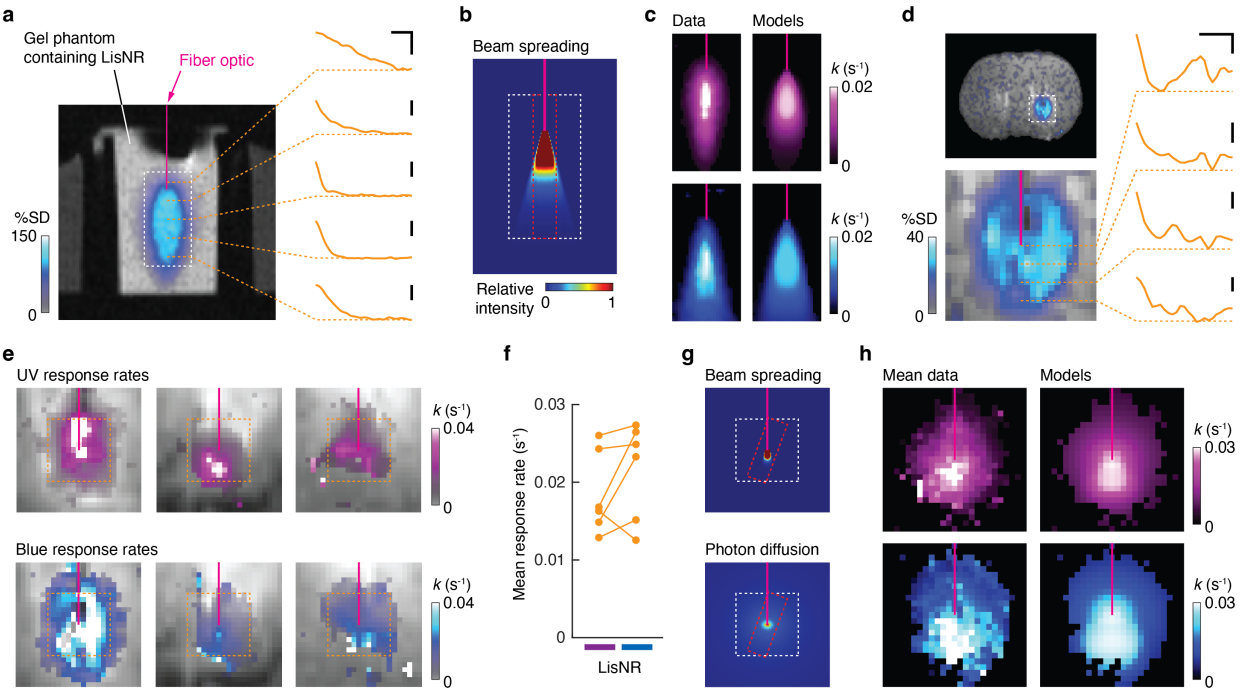

Fig. 4 | Light mapping using LisNRs. a, Image showing distribution of signal differences upon blue illumination (color) of a phantom formulated with Light-LisNRs in 1% agarose. Position of fiber optic is shown in magenta. Time courses at right are drawn from voxel locations denoted by orange dashed lines. Scale bars = 120 s (horizontal) and 20% (vertical). Dashed rectangle denotes region over which response rate maps are calculated. **b,** Representative beam spreading profile computed for fibers with core diameter = 200 μm and numerical aperture = 0.39, as used for experiments here (fiber position in magenta). Dashed rectangles denote location of the experimental in-plane field of view (white) and slice orientations (red) with respect to the modeled profile. **c,** Comparison of response rate maps recorded (left) or modeled (right) for UV illumination (top) and blue illumination (bottom). Field of view corresponds to dashed rectangles in **a** and **b**. **d,** Coronal image (top) with closeup of dashed region (bottom) showing blue-induced signal difference (color) overlaid on data from an individual LisNR-injected rat; fiber location shown in magenta. Traces at right denote time courses from individual voxels denoted by orange dashed lines. Scale bars = 120 s (horizontal) and 5% (vertical). **e,** Light response maps computed from three individual animals over regions corresponding to the closeup in **d**, for UV (top) and blue (bottom) illumination. **f,** Mean k values from regions equivalent to orange dashed rectangles in **e** for six animals during UV and blue illumination. **g,** Representative beam spreading (top) and photon diffusion (bottom) profiles used to fit light response maps. **h,** Mean data (left, $n = 6$) and best-fit modeled (right) light response rate maps for UV (top) and blue (bottom) illumination computed over the image volume denoted by white (in-plane) and red (perpendicular to slice) dashed rectangles in **g**.

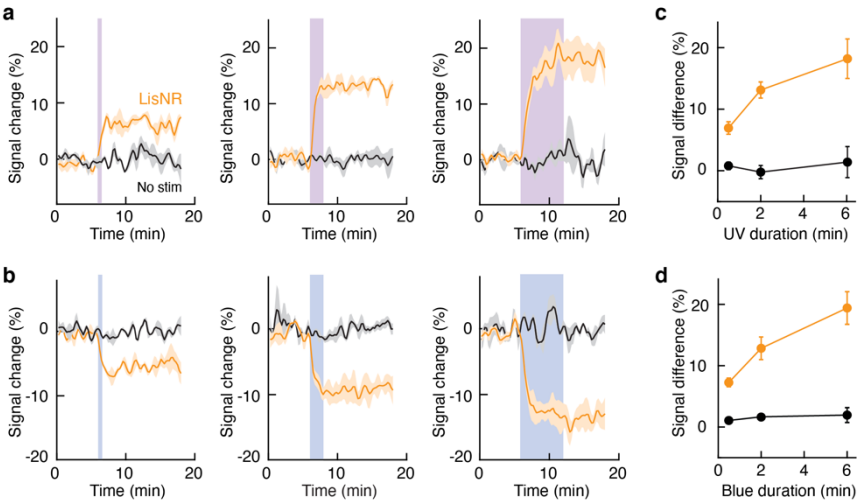

Extended Data Figure 1. Light-LisNR response as a function of stimulus duration. (a) MRI signal in response to UV irradiation of Light-LisNRs (orange) over varying durations: 0.5 min (left), 2 min (middle), and 6 min (right). Corresponding unilluminated control data shown in black. Shaded margins denote SEM of n = 3. **(b)** Equivalent time course data for blue illumination. **(c)** Signal differences observed following UV irradiation (orange) or control treatment (black) of LisNRs over the durations indicated. Error bars denote SEM of n = 3. **(d)** Equivalent signal difference data for blue illumination.

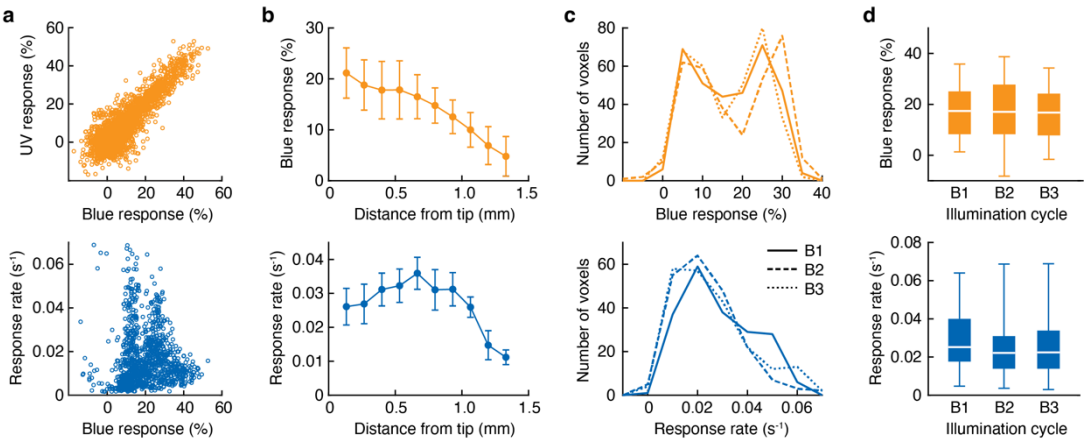

Extended Data Figure 2. Dissociation between light response rates and amplitudes. (a) Top: Light-LisNR response amplitudes to blue and UV light are highly correlated over a 25 x 25 voxel region around fiber optic tips in six animals ($R = 0.89$, $p < 10^{-5}$). Bottom: in contrast, blue light response amplitudes and response rates are statistically independent over the same voxels ($R = –0.013$, $p = 0.66$), indicating that the LisNR response rates are not strongly affected by variations in probe concentration, which largely determine the signal change amplitude distribution. **(b)** Response amplitudes and rates can also be dissociated from one another as a function of distance from the fiber tip: amplitudes decrease monotonically (top), while response rates peak and then diminish (bottom). **(c)** Histograms of blue light response amplitudes (top) and response rates (bottom) over three cycles of illumination (B1-B3), showing stability over time ($n = 2$ animals). **(d)** Box plots corresponding to the distributions in panel (c). Central line = median, box limits = first and third quartiles, whiskers = limiting values. Consistency of the distributions indicates that diffusion and convection over the ~1 hour experimental time period do not strongly affect the results.

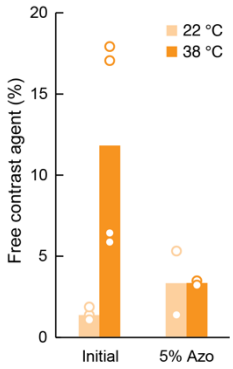

Supplementary Fig. 1 | Assessment of Gd^{3+} leakage from liposomal preparations. Quantification of free contrast agent as a percentage of total after incubation of LisNR formulations (2.2 mM Gd^{3+}) for 10 min at 22 or 38 °C. Concentrations were determined by ICP-MS following gel filtration chromatography to separate intact liposomes from free contrast agent. Results are presented for initial LisNR preparations and for LisNRs formulated with 5% AzoPC, 90% DPPC, and 5% DSPE-PEG,

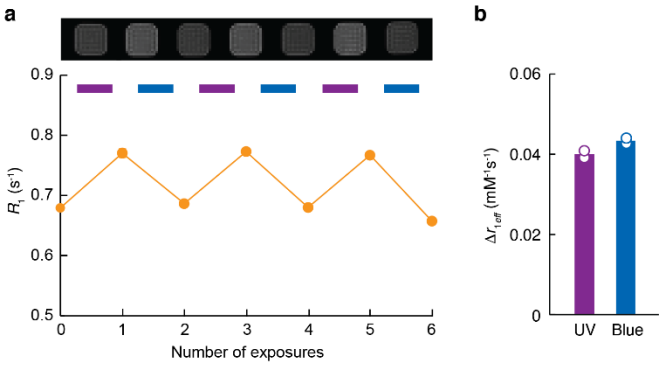

Supplementary Fig. 2 | Photosensitivity of LisNRs formulated with 5% AzoPC. a, Measurements of R_1 over repeated cycles of UV and blue illumination of LisNR specimens formulated with 5% AzoPC, 90% DPPC, and 5% DSPE-PEG. Corresponding T_1w MRI scans shown at top. Error bars denote SD of $n = 2$ technical replicates. **b,** Values of $\Delta r_{1\,eff}$ corresponding to the relaxation changes indicated in **a**.

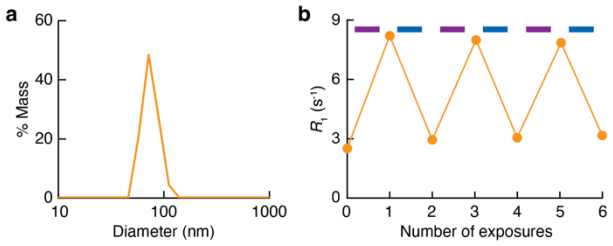

Supplementary Fig. 3 | Performance of small LisNRs. a, Dynamic light scattering size histogram showing size distribution measured from LisNRs formed using the composition of **Fig. 2d**, but extruded through a 50 nm-mesh membrane. The mean hydrodynamic diameter is 76 nm, with a polydispersity of 17%. **b,** R_1 values, measured under the conditions of **Fig. 2d** using the smaller LisNRs, over repeated cycles of UV and blue illumination.

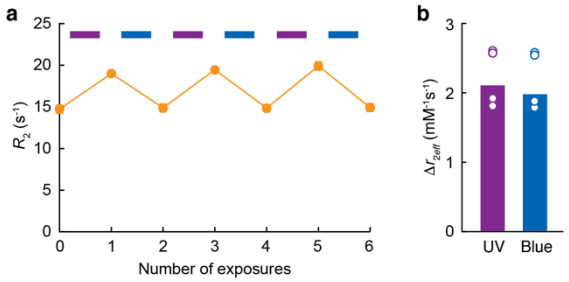

Supplementary Fig. 4 | Transverse relaxation effects of optimized Light-LisNRs. a, Transverse relaxation rates (R_2) measured under the conditions of **Fig. 2d** from the same optimized Light-LisNR preparations, over alternating cycles of UV and blue illumination (indicated at top). Error bars denote SD of n = 6 technical replicates. **b,** The change in effective transverse relaxivity (Δr_{2eff}) recorded after each UV or blue illumination period shown in **a**.

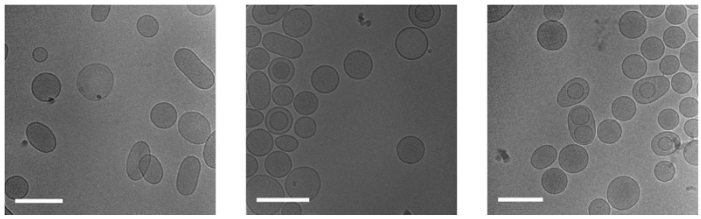

Supplementary Fig. 5 | Additional TEM images of optimized Light-LisNRs. Images acquired from three separate batches of Light-LisNRs, illustrating consistent characteristics analogous to those shown in **Fig. 2g**. Scale bars all 200 nm.

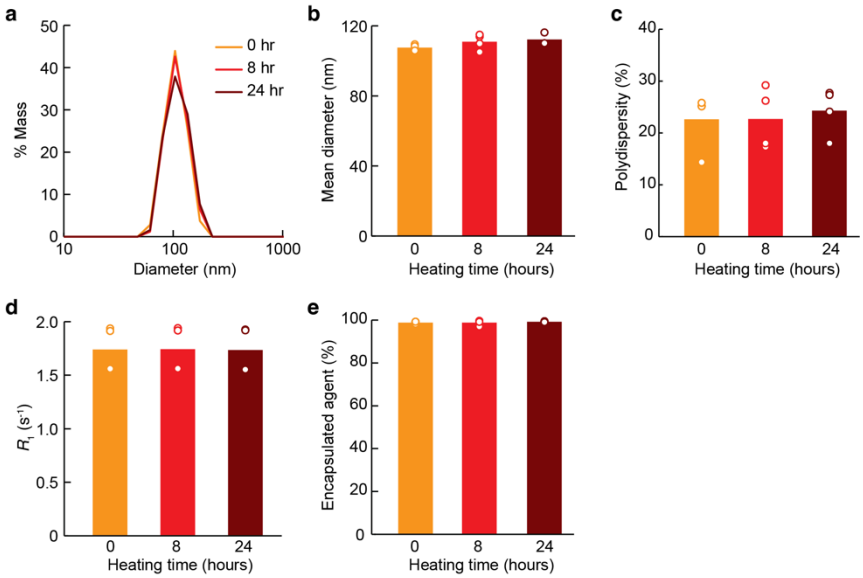

Supplementary Fig. 6 l Long-term stability of optimized LisNRs. a, Dynamic light scattering (DLS) size distribution histograms recorded from LisNRs incubated at 38 °C for 0, 8, or 24 hours, showing little change. **b,** Mean diameters recorded from the DLS data of panel **a**. **c,** Mean polydispersity values recorded from the experiments of panel **a**. **d,** R_1 values recorded from suspensions of LisNRs containing 2.2 mM Gd^{3+}, following incubation at 38 °C for the times shown. **e,** Measurements of the amount of contrast agent retained by the LisNRs following variable incubation at 38 °C, according to the leakage test of **Supplementary Fig. 1**.

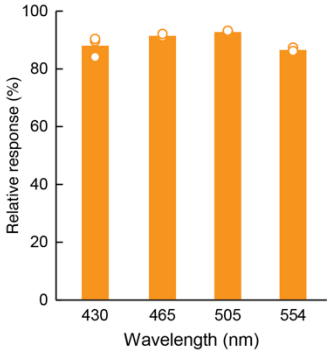

Supplementary Fig. 7 | Light-LisNR response to long wavelength illumination. Optimized 100 nm-diameter LisNR probes were preactivated with UV light and then stimulated with LED light sources operating at the wavelengths indicated and output powers ≥ 40 mW/cm^2 over 10 minutes. All tested wavelengths elicit substantial contrast responses.

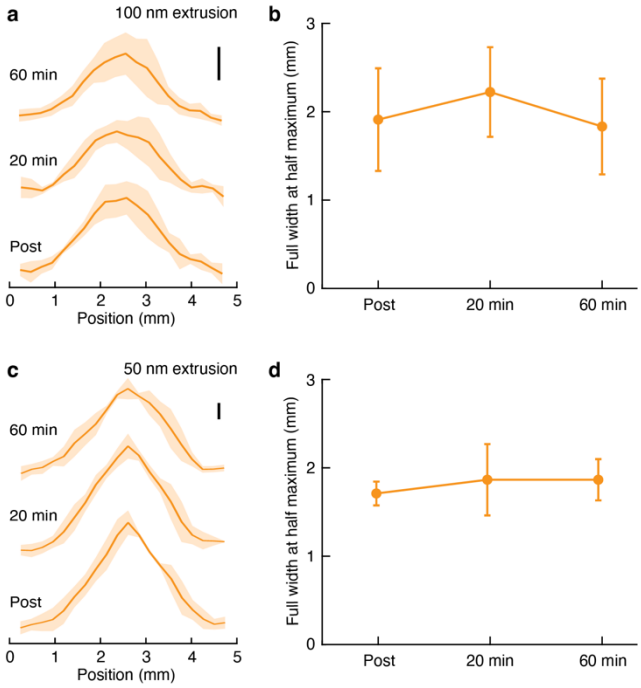

Supplementary Fig. 8 | Stability of injected LisNR distributions *in vivo*. a, Contrast enhancement by injected LisNRs as a function of lateral position, equivalent to profile in **Fig. 3b**, at multiple time points immediately (Post), 20 min, or 60 min after contrast agent infusion. These LisNRs were prepared using the standard 100 nm-mesh extrusion filter as in **Fig. 2**. Shading indicates SD for $n = 6$ biological replicates, vertical bar = 50% signal. **b,** Full width at half maximum (FWHM) values for contrast enhancements observed at each time point, showing approximate stability over time. Error bars denote SD of $n = 6$ biological replicates. **c,** Data equivalent to **a**, but obtained following injection of smaller LisNRs formulated using a 50 nm extrusion mesh rather than the standard 100 nm mesh. Shading denotes SD of $n = 3$ biological replicates, vertical bar = 50% baseline signal. **d,** FWHM values corresponding to the data in panel **c**. Error bars denote SD of $n = 3$ biological replicates.

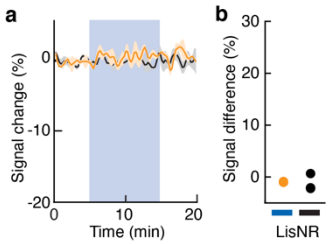

Supplementary Fig. 9 | Blue light insensitivity of Light-LisNRs after injection. a, Signal change *vs.* time before, during, and after initial blue irradiation (blue shading) of injected Light-LisNRs (orange), with time course of corresponding unstimulated LisNRs shown in black. Shading denotes SEM of $n = 3$ biological replicates. **b,** Mean signal differences produced during initial blue illumination (blue) or illumination-free control treatment (black) in LisNR-injected brain regions.

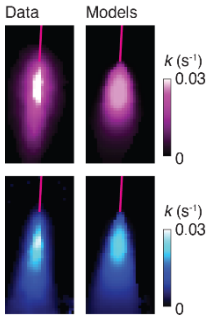

Supplementary Fig. 10 l Reproducibility of light mapping data in phantoms. Comparison of light response rate maps recorded (left) or modeled (right) for UV illumination (top) and blue illumination (bottom) from a second phantom, formulated similarly to the one featured in **Fig. 4** and revealing results similar to those in **Fig. 4c** over an equivalent field of view.